GPS Solutions (2024) 28:123
https://doi.org/10.1007/s10291-024-01662-2

ORIGINAL ARTICLE

Automated offset detection approaches: case study in IGS Repro2 and 3

Jin Zhang[1,2] · Lizhen Lian[3] · Chengli Huang[3,2,4] · Cancan Xu[1,4] · Simeng Zhang[1,4]

Received: 27 December 2023 / Accepted: 12 April 2024 / Published online: 13 May 2024

Abstract

Traditional automated offset detections on global navigation satellite system (GNSS) station coordinate time series still cannot fully replace manual detections in practical applications due to their high false positive detection rates. We developed preliminary and enhanced offset detection approaches and tested them against the solutions from the International GNSS service 2nd and 3rd data reprocessing campaigns (Repro2 and Repro3). Their manually detected offset recordings in International Terrestrial Reference Frame (ITRF) 2014 and ITRF2020 are used as evaluation criteria. In the preliminary approaches, stochastic models based on covariance matrix, white noise model, and white noise plus flicker noise model of both univariate and multivariate are studied. Although we achieved true positive, false positive, and false negative (TP, FP, FN) rates of (0.44, 0.40, 0.16) for Repro2 and (0.42, 0.44, 0.13) for Repro3, the preliminary automated detections still lead to many false positive detections. Thus, based on the preliminary approaches, and ancillary data, an enhanced detection approach is proposed. Enhanced detections significantly reduce 56%~80% false positive detections compared to preliminary approaches. As a result, for Repro3, the optimal overall performance is attained with (TP, FP, FN) rates of (0.57, 0.25, 0.18), along with a detection rate of 75%; for Repro2, the rates are (0.58, 0.20, 0.22), accompanied by a 73% detection rate. The current enhanced approach may serve as a supplementary or reference to manual detection, although still not being perfect. Furthermore, 20 manually detected unknown offsets in ITRF2020 are found to correspond to some known events (13 earthquakes and 7 equipment changes); 34 automated detections that correspond to known events but are not collected in ITRF2020 are manually checked as offsets (14 earthquakes and 20 equipment changes).

Keywords Automated offset detection · Noise analysis · Multivariate analysis · ITRF

Introduction

Nearly 40 years of observational data from the global navigation satellite system (GNSS) permanent station have been accumulated since the 1980s. Based on the accurate velocity and uncertainty estimation of these time series, many geodetic and geophysical applications and phenomena could be researched, such as global and regional reference frame realization, plate tectonic deformation, glacial isostatic adjustment, and crustal loading deformation (Bock and Melgar 2016; Herring et al. 2016). In the increasing number of stations and longer time series, offsets that occur at a high frequency and potentially stem from various causes can damage the accuracy of estimating velocities (Williams 2003b; Griffiths and Ray 2015; Lian et al. 2018). Especially, known and unknown offsets covered in noise is an obstacle to the scientific research objectives of 0.1 mm/y velocity uncertainty.

✉ Lizhen Lian
lianlizhen@shao.ac.cn

✉ Chengli Huang
clhuang@shao.ac.cn

[1] Shanghai Astronomical Observatory, Chinese Academy of Sciences, Shanghai 20030, China

[2] School of Physical Science and Technology, ShanghaiTech University, Shanghai 201210, China

[3] CAS Key Laboratory of Planetary Sciences, Shanghai Astronomical Observatory, Chinese Academy of Sciences, Shanghai 20030, China

[4] School of Astronomy and Space Science, University of Chinese Academy of Sciences, Beijing 100049, China

Detecting discontinuities has been a pivotal task in the preprocessing analysis during the establishment process of the international terrestrial reference frame (ITRF). The ITRF is constructed based on the long-term continuous observations of four space geodetic techniques: very long baseline interferometry (VLBI), global navigation satellite system (GNSS), satellite laser ranging (SLR), and Doppler orbitography and radiopositioning integrated by satellite (DORIS). To establish and maintain the ITRF, each technique's analysis center submits solutions utilizing the latest models and strategies to its combination center. IGS Repro2 and Repro3 are combined solutions of GNSS, specifically used to establish ITRF2014 and ITRF2020, respectively. Currently, the ITRF is a long-term solution that requires estimating station velocities as accurately as possible. However, during the observational process spanning many years, stations may experience discontinuities due to earthquakes (EQ), antenna changes (AT), receiver changes (RE), non-linearity (NL, such as ice melting), unknown reasons (UK), and so forth, resulting in abrupt changes in station coordinates. Presently, the method for handling these abrupt changes involves accurately detecting their occurrence epochs in the time series and conducting segmented fitting.

However, detecting offsets perfectly is challenging. ITRF offsets (discontinuities) are visually inspected using external information from equipment changes in site logs and co-seismic deformation of registered earthquakes in the Global Centroid Moment Tensor Project (Altamimi et al. 2016, 2023). Although the well-known Detection of offsets in GPS Experiment (Gazeaux et al. 2013, DOGEx) indicated that manual methods (where offsets are hand-picked) almost always gave better results than automated or semi-automated methods, it is essential to note that manual methods still suffer from high false detection rates and are not efficient enough. Thus, effective and stable automated offset detection algorithms are highly important and have been the research focus over the years.

Generally, offsets as a bias in GNSS times series analysis are investigated on two aspects: offset influence and offset detection. First, the influence of offsets to model parameter estimates depends on different observational noise types (Williams 2003a; Williams et al. 2004; Wang and Herring 2019), the positions of the offsets within the time series (Perfetti 2006) and the offset magnitudes. Even though growing offset numbers could increase the velocity uncertainties, offsets remaining undetected could have worse impacts (Williams 2003a; Gazeaux et al. 2013). Therefore, the recommended way is to estimate velocities, offsets, and noise components simultaneously (Williams 2003b; Perfetti 2006).

Concerning on offset detection, various offset detection methods and procedures have been investigated, including finding outliers and discontinuities in time series (FODITS) in Bernese by Ostini et al. (2008), Sigseg by Vitti (2012), L1 regularization by Wu et al. (2018), STARS by Bruni et al. (2014), multivariate analysis by Khazraei and Amiri-Simkooei (2021). However, the performance of these offset detection methods on real data has not been extensively researched. Actually, there are only a few studies on the application performance of automated offset detection in real data and their findings are reviewed as follows.

Perfetti (2006) applied classical detection identification adaptation (DIA) method (Teunissen 1998) to detect offsets in the Italian GNSS Fiducial Network. When an offset candidate is detected by DIA, it will be checked manually, and as a result 70% of the offsets are identified. However, it is worth noting that Perfetti (2006) only utilized data from 8 real stations, if the station number increase, manual checking becomes inefficient. Najder (2020) used 10 real stations to investigate the confidence level of automated offset detection for FODITS, the results indicate that false detections almost damage the automated detections. Similar results can be found in Gazeaux et al. (2013). Most recently, Lahtinen et al. (2021) proposed a semi-automatic offset detection method and achieved a detection performance of 49% for true positive (TP), 15% for false negative (FN), and 35% for false positive (FP), compared to manual detection results. Generally, Lahtinen et al. (2021) have attained superior outcomes with real datasets until now. However, their FP rate remains relatively high, and the data included 268 stations in Nordic Geodetic Commission (NKG) rather than global network.

Furthermore, regarding on improving the automated offset detection, several studies have been conducted. Amiri-Simkooei et al. (2018) consider colored noise and apply the multivariate analysis method in offset detection. They conclude that ignoring flicker noise existing in the time series will lead to lower offset detection performance. However, Lahtinen et al. (2021) find that small-size offsets, behaving like flicker noise, can remain undetected if flicker noise model is used. Consequently, they only applied the white noise model. Further investigation is required to determine which noise model should be utilized.

This work aims to propose a globally applicable and automated offset detection method on real datasets. We take advantage of the classical DIA method to detect offsets and simultaneously estimate velocity parameters, offset magnitudes, and their uncertainties. The DIA method, originating from Teunissen (1985, 1990), has been further explored by Teunissen (2017), Zaminpardaz and Teunissen (2019), and Yang et al. (2021). Additionally, in order to study the impact of noise on offset detection, we employ the noise analysis method proposed by Amiri-Simkooei et al. (2018), which focused on the least square estimates of noise

component for both univariate and multivariate. The theory and applications of the multivariate analysis are presented in Amiri-Simkooei (2008) and Amiri-Simkooei et al. (2007, 2017, 2018).

The rest of this paper is organized as follows. "Fundamental theories" section briefly reviews the fundamental theories used in this study. "Data introduction" section introduces the utilized data. "Detection approaches" section presents numerical preliminary automated detection approaches, results, and analysis to discuss the performance of offset detection in real data, as well as the impact of the noise model and coordinate component. "Results and analysis" section proposes enhanced detection approaches based on preliminary findings and utilizing ancillary data. Finally, "Conclusion" section concludes the study.

Fundamental theories

The proposed approaches are based on hypothesis testing and noise analysis, fundamental theories are briefly reviewed here.

Functional model

Traditional functional model of GNSS time series takes consideration of the deterministic effects: a linear trend generally caused by plate tectonic deformation, potential periodic signal caused by geophysical effects, and known offsets caused by various reasons, it is written as

$$y(t_i) = D + v \cdot t_i + \sum_{j=1}^{n} A_j \cdot \cos\left(\omega_j t_i + \varphi_j\right) + \sum_{k=1}^{n_g} g_k \cdot C(t_i - T_k) \tag{1}$$

where $y(t_i)$ is the station coordinates at time t_i, D is the intercept, v means the station velocity; A_j, ω_j, and φ_j refers to the amplitude, frequency, and phase of the j-th harmonic; n is the harmonic number; g_k and T_k is the magnitude and occurrence moment of the kth offsets; n_g is the number of offsets and $C(t_i - T_k)$ is the step function where $C=0$ for $t_i < T_k$ and 1 for $t_i \geq T_k$. Annual and semiannual period components are used in this work.

Stochastic model

Covariance-based stochastic model

In this paragraph, we introduce how to define the stochastic model based on covariance (COV) matrices. The computed COV for X, Y, and Z components of station s at time t_i are converted to the local reference system through the error propagation law. Since the applied data is already expressed in the same reference frame, no further transformation is required. The resulting stochastic model for station s becomes:

$$\mathbf{COV}_s = \begin{bmatrix} \mathbf{COV}_{enu}(t_1) & \cdots & 0 \\ \vdots & \ddots & \vdots \\ 0 & \cdots & \mathbf{COV}_{enu}(t_n) \end{bmatrix} \tag{2}$$

$\mathbf{COV}_{enu}(t_i)$ refers to the variances of east, north, or up component at time t_i.

Noise-based stochastic model

To construct the noise-based stochastic model, several prior studies have been referred to. As like many geophysical phenomena, the power spectra of noise in GNSS time series can be effectively approximated by

$$P(f) = P_0 f^{-\alpha} \tag{3}$$

where P_0 is a constant, α is the spectral index (0 for white noise, 1 for flicker noise, and 2 for random walk noise), f is the frequency (Agnew 1992). The Fractional Brownian motion is described in more detail in e.g. Zhang et al. (1997), Mao et al. (1999) and Williams et al. (2004). The noise structure is found to be a combination of white noise (WN) and flicker noise (FN) for the majority of GNSS time series (Zhang et al. 1997; Amiri-Simkooei 2008).

Then, the least square variance component estimate (LSVCE) methods proposed by Amiri-Simkooei (2008) are applied to estimate the noise component on both univariate and multivariate. For brevity, the multivariate form is reviewed first and then the univariate form is given as a special case. Assuming a linear model of observation equations formed as:

$$\begin{aligned} &\mathrm{E}(\mathrm{vec}(\mathbf{Y})) = \left(\mathbf{I}_r \otimes \mathbf{A}\right)\mathrm{vec}(\mathbf{X}) \\ &\mathrm{D}(\mathrm{vec}(\mathbf{Y})) = \mathbf{Q}_{\mathrm{vec}(\mathbf{Y})} = \boldsymbol{\Sigma}\otimes\mathbf{Q} = \boldsymbol{\Sigma}\otimes\sum_{p=1}^{p_0}\sigma_p^2\mathbf{Q}_p \end{aligned} \tag{4}$$

where $\mathrm{E}(\cdot)$ is the expectation operator, $\mathrm{D}(\cdot)$ is the dispersion operator, $\mathrm{vec}(\bullet)$ is the vector operator, $\mathbf{A}$ is the design matrix based on equation (1), $\otimes$ is the Kronecker product, $\mathbf{I}_r \in \mathbb{R}^{r\times r}$ is the r-dimension identity matrix, $\mathbf{Y} \in \mathbb{R}^{n\times r}$ is the observable matrix, $\mathbf{X} \in \mathbb{R}^{m\times r}$ is the matrix of unknown parameters, $\mathbf{Q}_{\mathrm{vec}(\mathbf{Y})} \in \mathbb{R}^{nr\times nr}$ refers to the variance matrix of$\mathbf{Y}$, and $\boldsymbol{\Sigma} \in \mathbb{R}^{r\times r}$ refers to the to-be-determined correlation matrix of r time series. $\mathbf{Q} \in \mathbb{R}^{n\times n}$ is the cofactor matrix and is expressed as a linear combination of cofactor matrix $\mathbf{Q}_p \in \mathbb{R}^{n\times n}$. $\boldsymbol{\sigma}_p^2$, $p = 1, \cdots, p_0$ are the unknown noise variance components to be estimated. When r=1, this formulation reduces to the univariate model. The noise structures of the

r components are assumed to be the same here. As the noise structure adopted in this contribution is a linear combination of white noise plus flicker noise (WFN). According to Zhang et al. (1997) and Amiri-Simkooei (2008), the assumed cofactor matrices is given by $\mathbf{Q} = \sigma_w^2\mathbf{Q}_w + \sigma_f^2\mathbf{Q}_f$, where $\mathbf{Q}_w$,$\mathbf{Q}_f$, σ_w^2, and σ_f^2 are the cofactor matrices and the variance components of WN and FN, respectively. Thus, $\boldsymbol{\sigma}^2 = \left[\sigma_w^2\sigma_f^2\right]^T$ reads

$$\boldsymbol{\sigma}^2 = \mathbf{N}^{-1}\boldsymbol{l} \tag{5}$$

where $\mathbf{N} \in \mathbb{R}^{2\times2}$ and $\boldsymbol{l} \in \mathbb{R}^2$. can be obtained by

$$N_{pq} = \frac{r}{2}\mathrm{tr}\left(\mathbf{Q}^{-1}\mathbf{W}_{\mathrm{A}}^{\perp}\mathbf{Q}_p\mathbf{Q}^{-1}\mathbf{W}_{\mathrm{A}}^{\perp}\mathbf{Q}_q\right), l_p = \frac{1}{2}\mathrm{tr}\left(\hat{\mathbf{E}}^T\mathbf{Q}^{-1}\mathbf{Q}_p\mathbf{Q}^{-1}\hat{\mathbf{E}}\boldsymbol{\Sigma}^{-1}\right) \tag{6}$$

where $\mathrm{tr}(\bullet)$ is the trace operator, $p, q = 1, 2$, $\mathbf{W}_A^{\perp} = \mathbf{I} - \mathbf{A}\left(\mathbf{A}^T\mathbf{Q}^{-1}\mathbf{A}\right)^{-1}\mathbf{A}^T\mathbf{Q}^{-1}$ is an orthogonal projector, and $\boldsymbol{\Sigma} = \frac{\hat{\mathbf{E}}^T\mathbf{Q}^{-1}\hat{\mathbf{E}}}{m-n}$ ($\hat{\mathbf{E}} = \mathbf{W}_{\mathrm{A}}^{\perp}\mathbf{Y}$ is the least square residuals matrix).

For a univariate model, $\boldsymbol{\Sigma} = 1$,$r = 1$, and $\hat{\mathbf{E}} = \hat{\boldsymbol{e}}$ in equation (6) ($\hat{\boldsymbol{e}} = \mathbf{W}_{\mathrm{A}}^{\perp}\boldsymbol{y}$ is the least square residuals). Then, the variance matrix of $\boldsymbol{y}$ in equation (4) is expressed as $\mathbf{Q}_{yy} = \sigma_w^2\mathbf{Q}_w + \sigma_f^2\mathbf{Q}_f$, and $\boldsymbol{\sigma}^2 = \mathbf{N}^{-1}\boldsymbol{l}$ with $n_{pq} = \frac{1}{2}\mathrm{tr}\left(\mathbf{Q}_{yy}^{-1}\mathbf{W}_{\mathrm{A}}^{\perp}\mathbf{Q}_p\mathbf{Q}_{yy}^{-1}\mathbf{W}_{\mathrm{A}}^{\perp}\mathbf{Q}_q\right)$, $l_p = \frac{1}{2}\left(\hat{\boldsymbol{e}}^T\mathbf{Q}_{yy}^{-1}\mathbf{Q}_p\mathbf{Q}_{yy}^{-1}\hat{\boldsymbol{e}}\right)$.

Hypothesis testing

The offset and outlier detection approach theoretically based on hypothesis testing, similar test theory can be referred to Teunissen (2017) and Amiri-Simkooei et al. (2018).

The null hypothesis H_0 means what one believes to be valid and the alternative hypothesis H_k means that a misspecification is assumed occurred. For a r-dimension linear model, H_0 and H_k are usually formed as:

$$H_0 : \mathrm{E}(\mathrm{vec}(\mathbf{Y})) = \left(\mathbf{I}_r \otimes \mathbf{A}\right)\mathrm{vec}(\mathbf{X}) \tag{7}$$

$$H_k : \mathrm{E}(\mathrm{vec}(\mathbf{Y})) = \left(\mathbf{I}_r \otimes \mathbf{A}\right)\mathrm{vec}(\mathbf{X}) + \left(\mathbf{I}_r \otimes \boldsymbol{C}_k\right)\mathrm{vec}\left(\boldsymbol{G}_k\right) \tag{8}$$

where $\boldsymbol{C}_k \in \mathbb{R}^m$ is the mean shift matrix and $\boldsymbol{G}_k \in \mathbb{R}^{1\times r}$ is the functional model misspecification that impacts the mean of $\mathbf{Y}$.

The search for potential model misspecifications is carried out through an identification step under the alternative hypothesis. Once the vector $\boldsymbol{C}_k$ is determined, the alternative hypothesis is specified, and the test statistic for r-dimension multivariate model reads

$$T_k = \frac{\boldsymbol{C}_k^T\mathbf{Q}^{-1}\hat{\mathbf{E}}\boldsymbol{\Sigma}^{-1}\hat{\mathbf{E}}^T\mathbf{Q}^{-1}\boldsymbol{C}_k}{\boldsymbol{C}_k^T\mathbf{Q}^{-1}\mathbf{W}_{\mathrm{A}}^{\perp}\boldsymbol{C}_k} \tag{9}$$

for univariate, substitute $\boldsymbol{\Sigma} = 1$ and $\hat{\mathbf{E}} = \hat{\boldsymbol{e}}$ into equation (9) yields $T_k = \frac{\left(\boldsymbol{C}_k^T\mathbf{Q}_{yy}^{-1}\hat{\boldsymbol{e}}\right)^2}{\boldsymbol{C}_k^T\mathbf{Q}_{yy}^{-1}\mathbf{W}_{\mathrm{A}}^{\perp}\boldsymbol{C}_k}$.

The maximum value of T_k, denoted as $\max_k T_k$, corresponding to a specific epoch, is regarded as a potential offset candidate and is subjected to testing at a specified significance level α_0. Under the null hypothesis, the test statistics follow a central chi-squared distribution with r-degree of freedom. The null hypothesis will be accepted if $\max_k T_k < \chi^2_{\alpha_0}(r)$ and rejected if $\max_k T_k \geq \chi^2_{\alpha_0}(r)$ If the alternative hypothesis H_k is accepted, adjustments to the null hypothesis are required to eliminate model misspecifications in the solution. Identified outliers are excluded, and detected offsets are incorporated into the function model. Subsequently, the null hypothesis is changed accordingly. The testing procedure is iterated until no outliers or offsets can be identified.

Based on the above basic principles, the unified detection procedure is as follows: First, establish functional and stochastic models. Second, starting from the 2nd observation epoch, iterate through all remaining epochs to compute T_k and find$\max_k T_k$. If $\max_k T_k \geq \chi^2_{\alpha_0}(r)$, it is considered as the existence of outliers or offsets. Remove the outliers or incorporate the offsets into the functional model. Then, return to the first step to re-establish the models and continue the detection process until $\max_k T_k < \chi^2_{\alpha_0}(r)$ in the second step.

Data introduction

IGS Repro2 and Repro3 represent the second and third reprocessed campaigns which combine the contributions from various analysis centers to establish ITRF2014 and ITRF2020. To evaluate the performances of our automated detection approaches, manually detected offset recordings in ITRF2014 and ITRF2020 are used as ground truth. Weekly solutions are used in this work rather than daily solutions. In general, the coordinates of a station are considered unchanged within a week, hence weekly solutions are derived from the combination of solutions from seven days of the week. Weekly solutions also have practical applications such as JPL Kalman filter and smoother realization of the International Terrestrial Reference Frame 2014 (JTRF2014). Therefore, our main focus is currently on weekly solutions. However, it should be noted that daily solutions and weekly solutions differ in noise characteristics. We hope to further analyze daily solutions based on the current work in the future. The URLs for the relevant data are provided in the Data availability section.

The features of offsets should be taken into consideration, including offset reasons, offset numbers, offset occurrence, and offset spatial and magnitude distributions. Regarding the reasons for offsets, there are five main categories: earthquakes, antenna changes, receiver changes, unknown reasons, and nonlinearities. Other minor causes, such as volcanic activities and cable repairs, are not analyzed here. Specifically, the statistical information of offsets in Repro2 and Repro3 are listed in Table 1. 72 stations were excluded from Repro2 and 11 stations were excluded from Repro3 because their corresponding codes could not be found in the ITRF discontinuity files based on the code field in the weekly solution files. The frequency of offsets, calculated following Williams(2003b) by offset numbers dividing the combined data span, occurs every 4 years for Repro2 and every 6 years for Repro3. In reality, offsets increase at an accelerated pace with the growing number of stations and equipment changes, highlighting the importance of an effective automated offset detection procedure.

As to the offset spatial and magnitude distributions, we present the Repo3 offset recordings in Fig. 1a and b. From Fig. 1b, we can see that different offset reasons and coordinate components indicate distinct magnitude distribution characteristics: the distribution dispersions of offsets caused by receiver change and non-linearity is smaller compared to that of unknown, antenna change, and earthquake in the two horizontal components. Notably, offsets caused by earthquake exhibiting the maximum dispersion in the horizontal components. In contrast, in the vertical components, offsets caused by earthquake have the smallest dispersion. Actually, offset magnitude is highly correlated with the detection rates, and we will elaborate this point in the following content.

Detection approaches

The preliminary detection approaches

Preliminary detection approaches are grounded in the fundamental theories introduced in "Fundamental theories" section. In order to assess the detection performance and evaluate the influence of both the noise (stochastic) models and the coordinate components, thirteen experiments are designed and listed in Table 2, along with their designated codes. Specifically, 3 types of noise models are constructed, including COV (covariance), WN (white noise), and WFN (white noise plus flicker noise); 4 coordinate components are considered, namely E, N, U, and multivariate (M), where multivariate consider east, north, and up simultaneously. Both univariate and multivariate models are included in WN and WFN. As a result, the former eleven experiments are designed and tabulated in Table 2.

The latter two experiments 12 and 13 are designed upon the former results. We find that utilizing only the WN model in offset detection leads to significant over-segmentation when employing the test statistic in equation (9). Nevertheless, test statistics that consider penalties, such as Bayesian Information Criterion with fixed C (BIC_C, where the subscript C represents the stochastic model, see Bos et al. (2013) and Lahtinen et al. (2021)), can effectively mitigate this over-segmentation. Consequently, we introduce the 12-th experiment WN_M^P ('P' denotes penalties, 'M' denotes multivariate model) to incorporates BIC_C. As for the 13-th experiment, we calculate the intersection of the offset detection results from WN_M^P and WFN_M (detailed in notes for Table 2) to reduce false positive detections. If a detected offset epoch is identified in WN_M^P, and there are detections within ± 3-points (namely ± 3 weeks in case of weekly solutions) range in WFN_M, the epoch will be accepted in the intersect results.

The enhanced detection approaches

Based on the research in preliminary detections, we select WN_M^P, WFN_M, and $WN_M^P \cap WFN_M$ from the preliminary 13 experiments due to their overall better performances. However, their results still yield high FP rates. Considering the fact that most of the offsets correspond to known events, we propose enhanced detection approaches that utilize the ancillary data to improve the offset detection performance. To eliminate the influence of non-linearity, 124 and 38 stations which have offsets caused by non-linearity are excluded from the preliminary 996 and 666 stations for Repro3 and Repro2, respectively. The remaining ITRF manual offset recordings are listed in Table 3.

We collected ancillary data from site logs and earthquake catalogues to help identify offsets. Basic information on station antenna changes and receiver changes recorded in site logs are gathered from online resources. The earthquake

Table 1 Offset numbers classified by offset reasons and the total numbers are both filled in the table

Data set	EQ	UK	AT	RE	NL	Total	Stations	Solutions
Repro 2	536	313	779	108	54	1790	666	1100
Repro 3	676	566	1345	153	185	2925	996	1409

Furthermore, the number of stations that happened at least one offset and the number of weekly solutions are listed in the table. These offset recordings are sourced from ITRF2014 (Altamimi et al. 2016) and ITRF2020 (Altamimi et al. 2023)

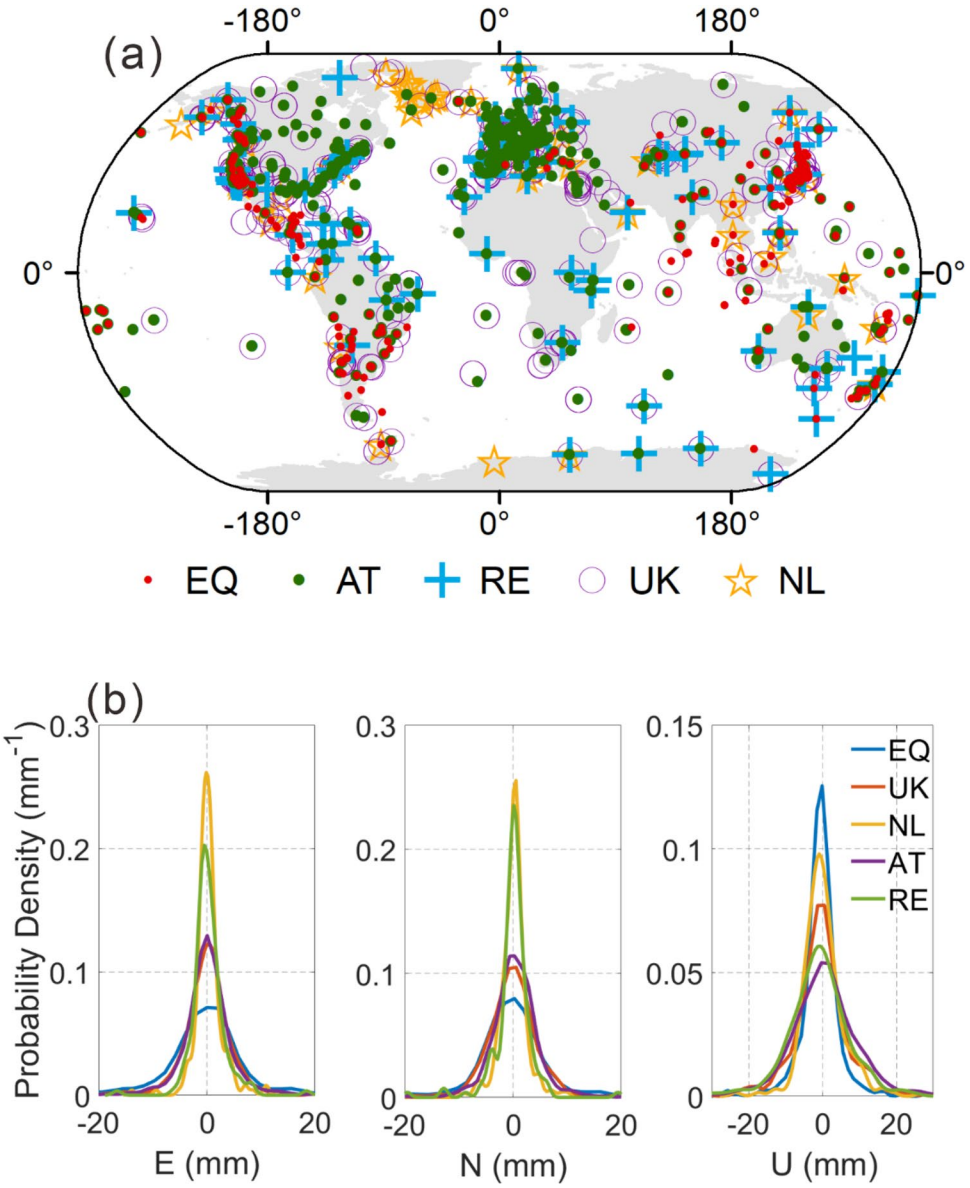

Fig. 1 The spatial and magnitude distribution of the offsets in Repro3. **a** The spatial distribution of offsets classified by reasons, namely EQ, AT, RE, UK, and NL. **b** The distribution of offset magnitudes in horizontal (E, N) and vertical (U) components categorized by the above five reasons, respectively

catalogues are established by Nevada Geodetic Laboratory (NGL) based on the following formula: $10^{\frac{M}{2}-0.79}$, where M is earthquake magnitude (Blewitt et al. 2018). We gathered 11,369 ancillary epochs for Repro3 and 5,318 for Repro2. Offset candidates detected within ± 3 points on both sides of these epochs will be considered as true offsets. Candidates that are not verified by the ancillary data will undergo additional testing using an enhanced test statistic. To confirm that no offsets indeed exist, the enhanced test statistic is also applied to the remaining ancillary epochs.

We choose the Sequential t-test analysis of regime shifts (STARS) from Bruni et al. (2014) as the enhanced test statistic, because STARS can identify offsets that exhibit clear step-change characteristics regardless of their positions in the time series. The theories of STARS are briefly reviewed here. An offset candidate x_j and its k-th right neighbor point x_{j+k} will undergo the test statistic: $m_1 + t\sqrt{2\delta_L^2/L} < x_{j+k} < m_1 - t\sqrt{2\delta_L^2/L}(k = 0, 1, \ldots, L-1)$, where, L is the window lengths, δ_L is the average standard deviation of all the possible L-point intervals, and t is the value of the t-distribution with $2L-2$ degrees of freedom at a given significance level β. At first, a mean m_0 and a standard deviation δ_0 are computed given equal weights to the left neighbor points $x_{j-k}(k = 1, 2, \ldots, L)$. Then, a weighted mean of the left neighbor data is calculated using weights defined on the basis of the Huber parameter$H$. We define

Table 2 The detection experiments are denoted by abbreviations: COV for covariance-based model, WN for white noise model, WFN for white noise plus flicker noise model, E, N, and U for east, north, and up, respectively

Experiment Number	Components	Stochastic model	Critical value	Code
1	E	COV	$\chi^2_{0.999}(1)$	$\mathrm{COV_E}$
2	N	COV	$\chi^2_{0.999}(1)$	$\mathrm{COV_N}$
3	U	COV	$\chi^2_{0.999}(1)$	$\mathrm{COV_U}$
4	E	WN	$\chi^2_{0.999}(1)$	$\mathrm{WN_E}$
5	N	WN	$\chi^2_{0.999}(1)$	$\mathrm{WN_N}$
6	U	WN	$\chi^2_{0.999}(1)$	$\mathrm{WN_U}$
7	ENU	WN	$\chi^2_{0.999}(3)$	$\mathrm{WN_M}$
8	E	WFN	$\chi^2_{0.999}(1)$	$\mathrm{WFN_E}$
9	N	WFN	$\chi^2_{0.999}(1)$	$\mathrm{WFN_N}$
10	U	WFN	$\chi^2_{0.999}(1)$	$\mathrm{WFN_U}$
11	ENU	WFN	$\chi^2_{0.999}(3)$	$\mathrm{WFN_M}$
12	**ENU**	**WN**	$\mathbf{BIC_C}$	$\mathbf{WN^P_M}$
13	**ENU**	**–**	**–**	$\mathbf{WN^P_M \cap WFN_M}$

M refers to multivariate that consider east, north, and up simultaneously. For instance, the experiment $\mathrm{WN_M}$ means applying the white noise model on multivariate components. For the initial eleven experiments, the test statistic is referenced to equation (9), while in the 12-th experiment $\mathrm{WN^P_M}$, a test statistic considering penalties (denoted by P), such as Bayesian information criterion with fixed C ($\mathrm{BIC_C}$, where the subscript C represents the stochastic model), is utilized to alleviate over-segmentation. The last experiment is the intersection of the offset detection results from $\mathrm{WN^P_M}$ and $\mathrm{WFN_M}$, denoted as $\mathrm{WN^P_M} \cap \mathrm{WFN_M}$

Table 3 Offset numbers classified by offset reasons and the total numbers in enhanced detections

Data set	EQ	UK	AT	RE	Total	Stations
Repro 2	501	301	741	99	1642	628
Repro 3	528	490	1204	126	2348	872

Furthermore, the numbers of stations, where at least one offset occurred, are listed in the last column of the table

$d_{j-k} = x_{j-k} - m_0$ and the weights of x_{j-k} will be set to 1 if $d_{j-k} < H\delta_0$, otherwise, d^{-1}_{j-k}. The final value m_1 is iteratively calculated by updating m_0 and δ_0. In this study, H is set to 3, and L is set to 10.

In summary, the enhanced detection process can be concluded in 3 steps:

Step 1: Matching offset candidates detected in the preliminary experiments with ancillary epochs, candidates within ± 3 points on both sides of these epochs are identified as offsets;

Step 2: Applying enhanced detections to the rest unidentified offset candidates, epochs of which meet the enhanced test statistic (i.e., STARS) will be identified as offsets;

Step 3: Applying enhanced detections to the rest ancillary epochs with no matching offset candidates, epochs meet the enhanced test statistic will be identified as offsets.

The enhanced detection experiments are denoted by the codes $\mathrm{WN^P_M}+$, $\mathrm{WFN_M}+$, and $\mathrm{WN^P_M} \cap \mathrm{WFN_M}+$, these experiments are also applied to both IGS Repro2 and Repro3 datasets. The detection results include the identified epochs with their corresponding site log events (antenna or receiver), earthquake events, or no events. The results are analyzed in the following content.

Results and analysis

Results and analysis of the preliminary detection approaches

Outliers

According to our results, around 1% to 2% of the observations are identified as outliers. The percentage of outliers detected by multivariate detection experiments are almost twice of the univariate detection experiments, because multivariate experiments simultaneously detect outliers across all three coordinate components. The slightly lower outlier detection rates for Repro3 compared to Repro2 may be attributed to less outliers within Repro3, considering its improvements in processing strategies.

Overall performance

To evaluate the overall performance, the true positive (TP), false positive (FP) and false negative (FN) rates had been counted as like Gazeaux et al. (2013). TP defines an offset that was collected in ITRF and also had been detected by our automated detection methods. More precisely, a TP is defined as a detected offset, the epoch of which is ± 3 points either side of an ITRF offset. FP refers to an offset not collected in ITRF but detected by our approaches. Finally, FN means an offset is collected in ITRF but has not been detected. Figure 2 illustrates the values of TP, FP and FN by their positions in a ternary plot which sum to 100 percent. Better performance will appear on the bottom right corner of the triangle. Moreover, we define detection rate as TP/(TP + FN).

It is evident that $WN_M^P \cap WFN_M$ performs the best, and achieves (TP, FP, FN) rates at (0.44, 0.40, 0.16) for Repro2 and (0.42, 0.44, 0.13) for Repro3. Then the performances of the rest experiments from high to low are WN_M^P, WFN_M, WFN (including E, N, U), COV and WN (including E, N, U), and WN_M. As to the influence of both the noise (stochastic) models and the coordinate components, we find that considering WFN model can improve the detection performance compared to COV and WN models. Multivariate detection approaches can almost detect all of the TP offsets detected by univariate approaches and achieve less FP detections. On the other hand, if we only use WN model, experiment with penalties WN_M^P is recommended to reduce FP detections and over-segmentation, and WN_M^P performs similar to WFN_M in TP and FN rates, but achieve lower FP rates. The intersection of WN_M^P and WFN_M can further improve the detection performance. From this, we observe that, aside from offsets, offset-like bias detected by WN_M^P and WFN_M are not entirely consistent.

To evaluate the results of the preliminary detections, we can review some previous studies. Bruni et al. (2014) tested the offset detection performance of the STARS method on 50 synthetic time series, achieving (TP, FP, FN) rates of (0.48, 0.28, 0.24). Amiri-Simkooei et al. (2018) examined the application of multivariate analysis in offset detection by 500 synthetic time series and their study showed that when the simulated offset magnitudes ranged from 1 to 3 mm horizontally and 2 to 6 mm vertically, the best detection rate (TP/TP + FN) reached 87.1%. Additionally, when the simulated offset magnitudes ranged from 0.5 to 1.5 mm horizontally and 1 to 3 mm vertically, the best detection rate was 31.6%. Gazeaux et al. (2013) evaluated offset detection results submitted by laboratories worldwide on 50 synthetic time series. The best results were approximately (0.4, 0.2, 0.4) got by manual detection and approximately (0.35, 0.30, 0.35) got by automatic detection, with the automatic method being FODITS in Bernese by Ostini et al. (2008). Khazraei and Amiri-Simkooei (2021) improved the multivariate analysis method proposed by Amiri-Simkooei et al. (2018) using spline function theory and tested its performance on Gazeaux et al.'s synthetic time series, achieving (0.33, 0.32, 0.34). These are some detection results from simulated data. Moving on to real data, Lahtinen et al. (2021) detected offsets in time series from 268 stations, reaching (0.49, 0.35,

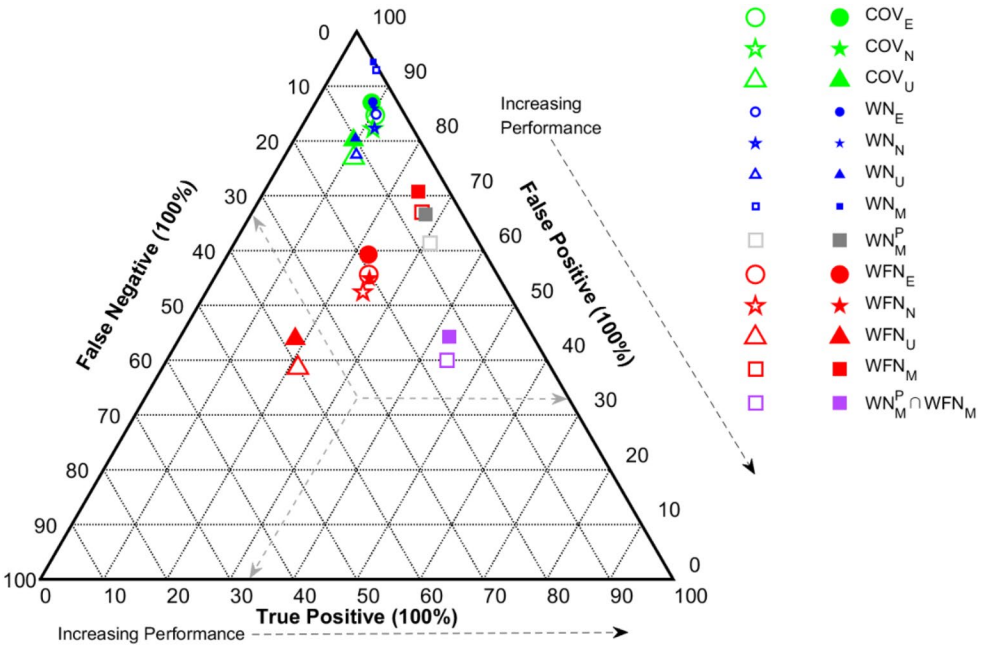

Fig. 2 TP, FP and FN rates of the 13 experiments in Table 1. Hollow and solid markers are used for IGS Repro2 and Repro3 respectively. Color green indicates COV-based stochastic model, color red refers to WFN stochastic model, blue color indicates WN stochastic model and purple color indicates WN detection approaches with penalties considered. Circle, pentagram, triangle and square refers to component E, N, U and multivariate respectively

0.16). It should be noted that due to differences in the data used and the descriptions of the results, direct comparisons cannot be made. However, based on the results of Gazeaux et al. (2013), we can adopt the criteria of a TP rate greater than 20%, an FN rate less than 40%, and an FP rate less than 40% to select relatively reliable offset detections. According to this threshold, Gazeaux et al.'s study shows that only two manually detected results, "NOCLMANL" and "SDPWMANL," and one automatic detection result, "AIUBCOD2," meet the requirement. As a result, our automatic detection results have, to some extent, reached a relatively high TP rate with a relatively low FN rate, but the FP rate is still somewhat high.

Figure 3 illustrates the detection rates of Repro3. WN_M^P, WFN_M, and $WN_M^P \cap WFN_M$ still perform better than other experiments. Although the detection rate of WN_M exceeds 90%, too many FP detections make it an unsuitable option. The most detectable offsets are caused by EQ, AT, and UK. Reviewing the magnitude distributions plot in Fig. 1b, we can say offset magnitude is highly correlated with the detection rates. However, it is important to note that we cannot conclude that offsets caused by unknown reasons are easier to detect, as ITRF only incorporates very clear offsets caused by unknown reasons, while smaller or less clear offsets may still be hidden in the time series. The lowest detection rate is in offsets caused by non-linearity. We should pay attention to this type of offset (more precisely, discontinuity), because nonlinearity in time series primarily manifests as the continuous change of velocity rather than abrupt jumps (Altamimi et al. 2016), and needs to be investigated separately. We also re-evaluated the performance of $WN_M^P \cap WFN_M$ after excluding stations where non-linearity offsets occurred, which slightly improved the performance, from (TP, FP, FN) rates at (0.44, 0.40, 0.16) and (0.42, 0.44, 0.13) to (0.46, 0.40, 0.14) and (0.45, 0.43, 0.12) for Repro2 and Repro3, respectively. That's to say, nonlinearity is not the primary reason for the high FP rate. Therefore, stations where nonlinearity offsets exist will be excluded in enhanced detections.

Results and analysis of the enhanced detection approaches

Overall performance

Results represent by TP, FP, FN rates are illustrated in Fig. 4, and the results from Lahtinen et al. (2021) are also included for comparison. But we should note that Lahtinen et al. used data from 268 stations in the Nordic Geodetic Commission, which differs from our work. As we can see in Fig. 4, the overall performances are improved significantly from preliminary to their enhanced detections. As a result, the best overall performance is achieved by the enhanced experiment $WN_M^P \cap WFN_M+$, with rates of (0.58, 0.20, 0.22) and (0.57, 0.25, 0.18) for Repro2 and Repro3, respectively. Based on our statistical analysis, the enhanced approach results in a 62% reduction in FPs for Repro2 and a 56% reduction for Repro3, amounting to 673 and 997 FP offsets, respectively, compared to the preliminary experiment $WN_M^P \cap WFN_M$. In the enhanced experiments WN_M^P+ and WFN_M+, FPs are reduced by 70% to 80%. However, it's noteworthy that a few TPs are also mistakenly excluded by the enhanced approaches. The decreasing of TPs can also be reflected by the declining detection rates as shown in Fig. 5 under the 'ALL' column. Specifically, the excluded TPs for $WN_M^P \cap WFN_M+$ are 53 (4%) and 75 (4%) for Repro2 and Repro3. The excluded TPs for WN_M^P+ and WFN_M+ range from 6 to 8%. By comparing the significantly reduced FPs

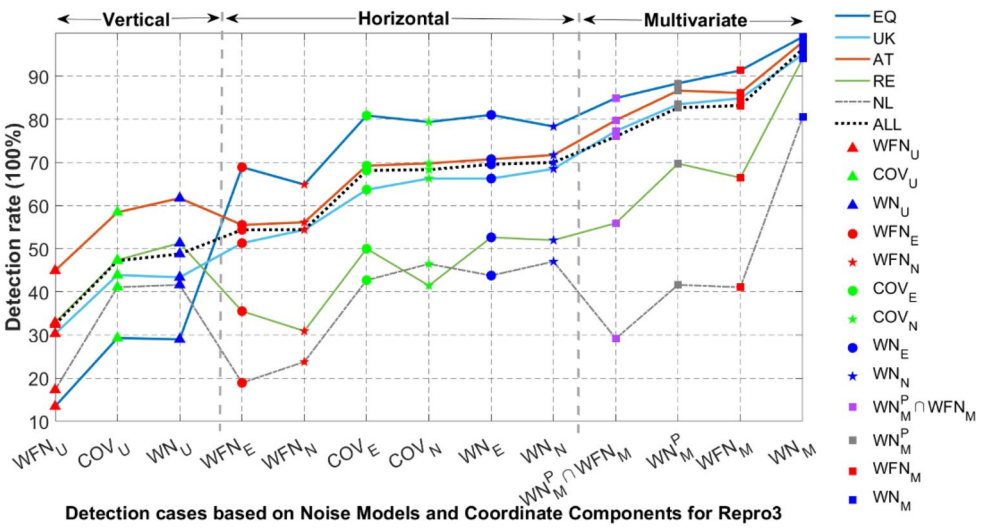

Fig. 3 Detection rates of the 13 experiments in Table 1 classified by offset reasons. EQ, UK, AN, RE, NL offsets are indicated by different type of lines and colors. The total detection rates of all offsets (ALL) are indicated in the dotted line. We only take Repro3 as an example because Repro2 performs similarly

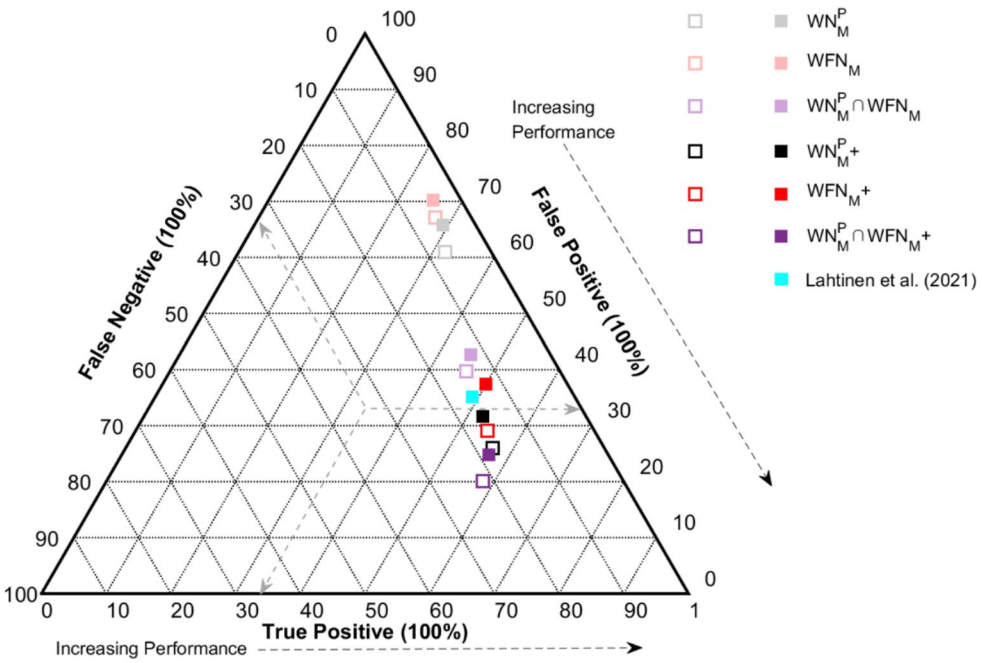

Fig. 4 TP, FP and FN rates of the enhanced detection experiments. Hollow and solid markers are used for IGS Repro2 and Repro3. Preliminary detection results and the results from Lahtinen et al. (2021) are also illustrated as comparison. Markers with dark color and light color represent enhanced detections and preliminary detections, respectively

and the slightly decreased TPs, we can conclude that our enhanced approaches demonstrate a substantial overall performance improvement.

Detection rates of the enhanced experiments for Repro3 are shown in Fig. 5, from which we can see, enhanced detection rates of EQ, AT, and RE offsets closely align with the preliminary experiment results, in contrast, UK offsets show nearly 20% (95 out of 490) decreasing. Essentially, offset detection is the process of identifying unfitted model biases, which are often intertwined with other errors, potentially leading to the misclassification of these errors as offsets. Therefore, achieving a perfect differentiation between offsets and other biases from detection results is challenging. With the help of ancillary data, we distinguish EQ, RE, AT offsets from detection results successfully. For detections without corresponding ancillary data, the enhanced detection approach excludes 1072 instances, out of which 95 pertain to UK offsets, and the remaining 977 are accurately excluded. As a result, almost 84% EQ, 80% AT, 60% UK, and 56% RE offsets are correctly identified.

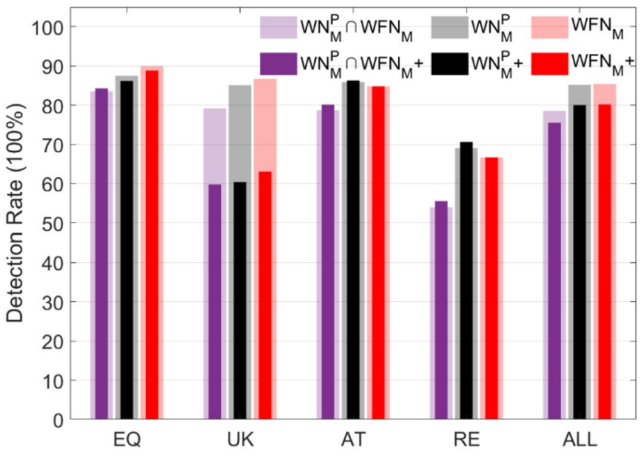

Fig. 5 Detection rates of the enhanced detection experiments classified by offset reasons (EQ, UK, AT, RE, and the sum of the four reasons, ALL). The preliminary detection results are also depicted with lighter-colored and wider bars for comparison. Repro3 is used as an illustrative example

FP detections and FN detections

To gain a deeper understanding of the automated detections, we provide an illustrative example in Fig. 6. Notably in Fig. 6a, an abrupt change occurring at the start of the time series remains unrecorded as an offset in the ITRF. Such observation errors may have been removed during the manual offset detection in ITRF. However, in automated detections, they are treated as outliers or offsets. These discrepancies underscore the distinctions between automated and manual detection strategies. FPs can be considered reasonable, as they provide valuable insights into potential offsets or other biases that require attention in the time series. Additionally, between 2000 and 2005 in Fig. 6a, two points were detected as offset candidates, and visually appeared to exhibit some discontinuous characteristics, but they were excluded after enhanced detection.

Two more examples are shown in Fig. 6b and c. From Fig. 6b, it can be observed that two offset candidates at the left end of the time series were excluded after enhanced

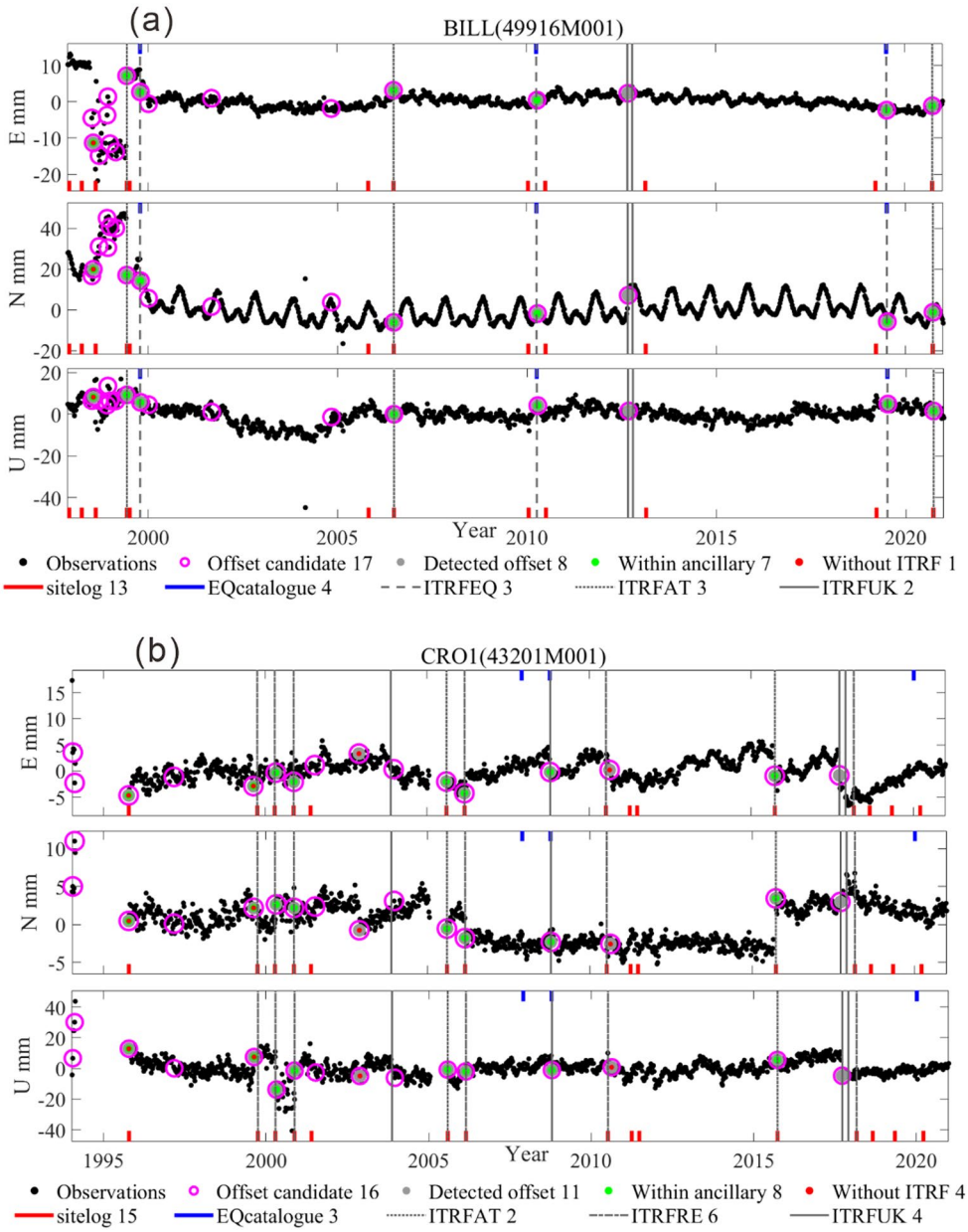

Fig. 6 Detection examples of station BILL (49916M001), CRO1 (43201M001), CUIB (41603M001). BILL, CRO1 and CUIB are the station codes and the number in parentheses is the DOMES number. Observations refer to residuals of E, N, U components after removing trend, annual and semiannual signals. The circles in pink represent offset candidates from $WN_M^P \cap WFN_M$. Gray dots refer to automated detection results of $WN_M^P \cap WFN_M+$, green dots refer to detections that correspond to known events, red dots refer to detections that not recorded in ITRF offsets. Short vertical lines in red and blue refer to equipment change epochs extract from site logs and EQ epochs documented in earthquake catalogues, respectively. ITRF offset epochs are represented by long vertical lines classified by offset reasons. The numbers in the legend correspond to the counts of the respective categories

detection, but the detection corresponding to the site log on the right side near 1995 was not recorded as an offset in the ITRF. An offset caused by unknown reasons on the left side near 2005 existed in the offset candidates but was excluded after enhanced detection. However, in the N direction, a significant offset point can be seen on the left side in 2005, which is not recorded in the ITRF.

From Fig. 6c, it can be seen that during the period from 2000 to 2005, an offset caused by earthquake was recorded in the ITRF but was not detected, while a more obvious jump detected near 2020, corresponding to the site log, was not recorded in the ITRF.

To evaluate the impact of the missed offsets (which correspond to FNs) on parameter estimations, which include velocities and the amplitudes of annual and semi-annual signals, we further take into account the FNs of $WN_M^P \cap WFN_M+$ and re-estimate these parameters. WFN models are still used here. The RMSs of the parameter differences between scenarios with or without FNs are then calculated and presented in Table 4. Consequently, the influence of FNs on velocity estimates is observed to be less than 0.1 mm/y horizontally and less than 0.2 mm/y vertically.

Manual check

We manually checked detections that correspond to ancillary data but are not consistent with ITRF offset recordings. As

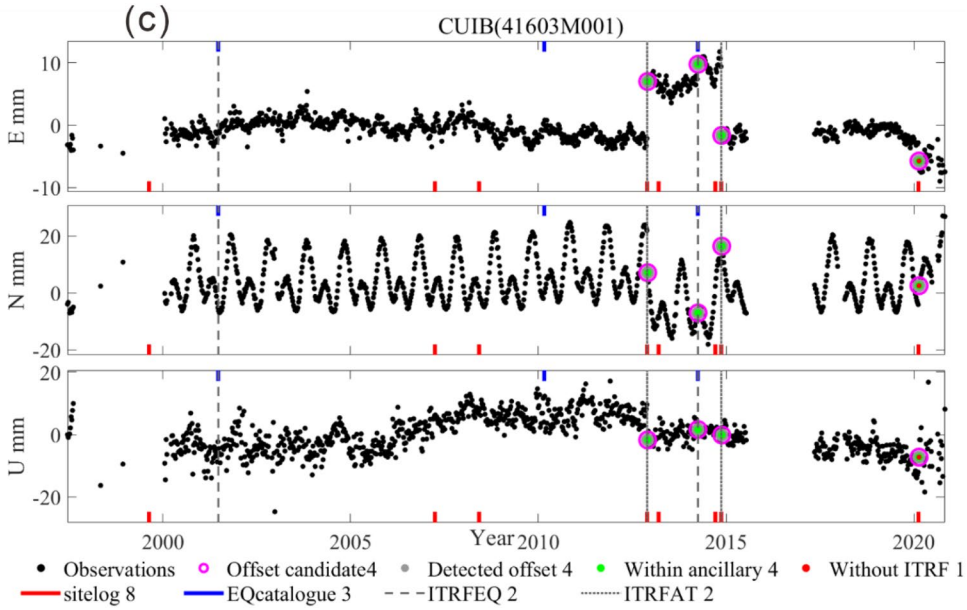

Fig. 6 (continued)

Table 4 RMSs of the parameter differences (including velocity and amplitudes of annual and semi-annual signals) between scenarios with or without FNs for $WN_M^P \cap WFN_M$

	IGS Repro3			IGS Repro2		
	E	N	U	E	N	U
Velocity (mm/y)	0.03	0.03	0.08	0.05	0.06	0.15
Annual (mm)	0.013	0.012	0.034	0.021	0.016	0.051
Semi-annual (mm)	0.005	0.006	0.019	0.011	0.008	0.026

a result, we identified 20 unknown offsets in ITRF2020 that align with known events (13 earthquakes and 7 equipment changes). Additionally, 34 automated detections that correspond with known events but are not collected in ITRF2020 are manually checked as offsets (14 earthquakes and 20 equipment changes). The details of these findings are provided in Appendix Tables 5 and 6.

Conclusion

This study introduces preliminary and enhanced automated offset detection approaches applied to IGS Repro2 and Repro3 datasets. Our results indicate that applying a white noise plus flicker noise (WFN) model significantly reduces false positive (FP) detections and can improve detection performance compared to the covariance-based stochastic model and white noise (WN) model.

Based on our research, several conclusions can be drawn. If we only use the WN model, penalties for adding parameters should be taken into consideration to avoid heavily FP detections. Multivariate detection approaches can almost detect all of the TP offsets detected by univariate approaches and achieve less FP detections. Furthermore, by combining the results from approaches utilizing the WFN and WN models, namely $WN_M^P \cap WFN_M$, we achieved somewhat "good" detections with (TP, FP, FN) rates of (0.42, 0.44, 0.13) for Repro3 and (0.44, 0.40, 0.16) for Repro2.

We further improved the detection performance by employing an enhanced approach that incorporates ancillary data and an extra test statistic. Our enhanced approaches exhibit a significant overall performance improvement compared to the preliminary methods, with a 60% reduction in FPs and a 4% decrease in TPs. The best overall performance is achieved by the enhanced approach, i.e., $WN_M^P \cap WFN_M+$ with rates of (0.57, 0.25, 0.18) and a 75% detection rate for Repro3 and rates of (0.58, 0.20, 0.22) with a 73% detection rate for Repro2. In comparison, results from Lahtinen et al. (2021) yielded rates of (0.49, 0.35, 0.16) with a 74% detection rate. Concerning the influence of FNs on velocity estimation for $WN_M^P \cap WFN_M+$, the RMSs of velocity differences between scenarios with or without FNs, are less than 0.1 mm/y horizontally and less than 0.2 mm/y vertically. Both our study and the research by

Lahtinen et al. (2021) have demonstrated the effectiveness of applying ancillary data in offset detection. Further research is needed to explore how to reduce false positive detections and obtain more reliable offset detection results.

Based on our study, despite certain inconsistencies in results between manual and automatic detection due to detection strategies and other factors, we have demonstrated the promise of applying automatic offset detection in real coordinate time series. We believe that the automated offset detection strategies we proposed have the potential to serve as valuable references and viable alternatives to the traditional manual approach. We can observe that the detection rate of offsets can reach 80% or even 90%. However, apart from velocity, period signals, white noise, flicker noise, and offsets, there may be many other model errors mixed in the real station time series. This is also the reason for the high false positive rate and is a problem that must be considered for more reliable, stable, and practical automated offset detection.

Appendix

See Tables 5 and 6.

Table 5 ITRF unknown offsets which are found correspond with known events

Code	EQ epoch	M	EQ name	Soln	Start epoch	End epoch
Unknown offsets correspond with EQ events						
AB21	14JUN23	7.9	usc000rki5	5	13:242:59103	14:175:00000
CKIS	09SEP29	8.1	usp000h1ys	1	00:000:00000	09:278:00000
CN00	16MAR19	6.0	us20005azy	3	15:032:19860	16:096:00000
CRO1	08OCT11	6.1	usp000gjyf	7	06:055:00000	08:290:00000
GUAM	20JUN23	5.9	us6000ahcr	4	19:066:03480	20:162:00000
GUUG	20JUN23	5.9	us6000ahcr	4	19:161:04020	20:162:00000
HKOH	11MAR11	9.1	official2011031 1054624120_30	2	10:222:00000	11:067:00000
KSMV	18JUL07	5.9	us2000fz0q	4	11:070:20783	18:175:00000
OWMG	16NOV13	7.8	us1000778i	1	00:000:00000	16:320:00000
TSK2	18JUL07	5.9	us2000fz0q	9	12:157:00000	18:167:00000
TSKB	18JUL07	5.9	us2000fz0q	11	11:242:05220	18:167:00000
VALP	08DEC18	6.2	usp000gqvv	2	01:099:32457	08:355:00000
ISHI	18JUL07	5.9	us2000fz0q	2	17:159:00000	18:177:00000

Code	Equipment change epoch	Equipment change reason	Soln	Start epoch	End epoch
Unknown offsets correspond with equipment change events					
AMC2	1999–09-01T15:43Z	Receiver	1	00:000:00000	99:238:00000
ANCG	2012–10-21T00:00Z	Antenna	1	00:000:00000	12:295:00000
CLAR	1996–09-12T00:00Z	Receiver	5	96:171:00000	96:247:00000
KOUR	2004–09-30T15:00Z	Receiver	4	02:030:00000	04:294:00000
RCM5	2004–02-20 T00:00Z	Antenna	1	00:000:00000	96:051:00000
SMO0	2018–05-02T09:00Z	Antenna	3	13:358:00000	18:122:00000
TIAS	2018–01-16T12:00Z	Antenna	1	00:000:00000	18:017:00000

There are two kinds of events, namely earthquake (EQ) and equipment change. Data regarding EQ events are sourced from the Nevada Geodetic Laboratory (NGL) earthquake catalogue, providing details such as EQ epoch, EQ magnitude (M), and EQ name. Information about equipment change events is extracted from site logs, which include the equipment changes epoch and the associated reasons for the changes. The fields 'Soln', 'Start epoch', and 'End epoch' are derived from the ITRF2020 discontinuity file

Table 6 Detections correspond with known events which are not recorded in ITRF

Code	EQ epoch	M	EQ name
Manually checked detections correspond with known EQ events			
DAEJ	04DEC26	9.1	official20041226005853450_30
DSMG	11MAR11	9.1	official20110311054624120_30
HKSC	11MAR11	9.1	official20110311054624120_30
HKSL	11MAR11	9.1	official20110311054624120_30
LHAZ	11MAR11	9.1	official20110311054624120_30
HKSC	12APR11	8.6	official20120411083836720_20
HKSL	12APR11	8.6	official20120411083836720_20
HNIS	16DEC17	7.9	us200081v8
IQQE	20DEC06	6.1	us7000cnnz
KARA	09JUL15	7.8	usp000gz8j
QUAR	09JUL15	7.8	usp000gz8j

Code	Equipment change epoch	Equipment change reason
Manually checked detections correspond with known equipment change events		
AHID	2000-12-20T00:00Z	Receiver
BAKO	1998-02-07T00:00Z	Receiver and antenna
CMP9	1997-01-28T00:00Z	Receiver
COSO	2018-03-30T20:58Z	Receiver
CSAR	2018-04-09T09:10Z	Receiver
CUIB	2020-02-13T14:59Z	Receiver and antenna
DWI1	2012-01-11T00:00Z	Receiver
KARL	2006-02-08T13:37Z	Receiver
KTVL	2017-01-09T14:59Z	Receiver
LONG	2015-11-18T18:48Z	Receiver
LONG	2017-02-14T20:24Z	Receiver
LURA	2016-12-14T23:59Z	Receiver
NKLG	2010-10-26T08:15Z	Receiver
PIN2	1997-09-21T00:00Z	Antenna
PRDS	2002-11-01T00:00Z	Antenna
SBRB	2011-04-15T18:29Z	Receiver
SMID	2020-03-17T16:15Z	Receiver
SVTL	2004-12-01T12:00Z	Receiver and antenna
URUM	2020-11-12T09:55Z	Receiver
WUHN	2018-05-05T00:00Z	Receiver

The fields in Table 6 are mirror those in Table 5

Acknowledgements This Study is supported by National Nature Science Foundation of China (Grants 12233010, 11903065).

Author contributions Jin Zhang did conceptualization, methodology, software, writing original draft. Lizhen Lian and Chengli Huang designed this research, did review and editing. All authors reviewed the manuscript.

Data availability The IGS repro2 and repro3 time series are available from the https://cddis.nasa.gov/archive/gnss/products/. The NGL earthquake catalogue data are obtained from http://geodesy.unr.edu/NGLStationPages/. The site log files are available from ftp://garner.ucsd.edu/pub/docs/station_logs/, ftp://ftp.geonet.org.nz/gps/sitelogs/logs/and ftp://igs.org/pub/station/log/.

Declarations

Conflict of interest The authors declare that they have no conflict of interest.

References

Agnew DC (1992) The time-domain behavior of power-law noises. Geophys Res Lett 19:333–336. https://doi.org/10.1029/91gl02832

Altamimi Z, Rebischung P, Métivier L et al (2016) ITRF2014: A new release of the International Terrestrial Reference Frame modeling nonlinear station motions. J Geophys Res: Solid Earth 121:6109–6131. https://doi.org/10.1002/2016jb013098

Altamimi Z, Rebischung P, Collilieux X et al (2023) ITRF2020: an augmented reference frame refining the modeling of nonlinear station motions. J Geodes 97:47. https://doi.org/10.1007/s00190-023-01738-w

Amiri-Simkooei AR (2008) Noise in multivariate GPS position time-series. J Geodesy 83:175–187. https://doi.org/10.1007/s00190-008-0251-8

Amiri-Simkooei AR, Tiberius CCJM, Teunissen PJG (2007) Assessment of noise in GPS coordinate time series: Methodology and results. J Geophys Res: Solid Earth 112:B7. https://doi.org/10.1029/2006jb004913

Amiri-Simkooei AR, Mohammadloo TH, Argus DF (2017) Multivariate analysis of GPS position time series of JPL second reprocessing campaign. J Geodesy 91:685–704. https://doi.org/10.1007/s00190-016-0991-9

Amiri-Simkooei AR, Hosseini-Asl M, Asgari J et al (2018) Offset detection in GPS position time series using multivariate analysis. GPS Solut 23:12. https://doi.org/10.1007/s10291-018-0805-z

Blewitt G, Hammond W, Kreemer C (2018) Harnessing the GPS data explosion for interdisciplinary science. Eos. https://doi.org/10.1029/2018eo104623

Bock Y, Melgar D (2016) Physical applications of GPS geodesy: a review. Rep Prog Phys 79:106801. https://doi.org/10.1088/0034-4885/79/10/106801

Bos MS, Fernandes RMS, Williams SDP et al (2013) Fast error analysis of continuous GNSS observations with missing data. J Geodesy 87:351–360. https://doi.org/10.1007/s00190-012-0605-0

Bruni S, Zerbini S, Raicich F et al (2014) Detecting discontinuities in GNSS coordinate time series with STARS: case study, the Bologna and Medicina GPS sites. J Geodesy 88:1203–1214. https://doi.org/10.1007/s00190-014-0754-4

Gazeaux J, Williams S, King M et al (2013) Detecting offsets in GPS time series: first results from the detection of offsets in GPS experiment. J Geophys Res: Solid Earth 118:2397–2407. https://doi.org/10.1002/jgrb.50152

Griffiths J, Ray J (2015) Impacts of GNSS position offsets on global frame stability. Geophys J Int 204:480–487. https://doi.org/10.1093/gji/ggv455

Herring TA, Melbourne TI, Murray MH et al (2016) Plate boundary observatory and related networks: GPS data analysis methods and geodetic products. Rev Geophys 54:759–808. https://doi.org/10.1002/2016rg000529

Khazraei SM, Amiri-Simkooei AR (2021) Improving offset detection algorithm of GNSS position time-series using spline function theory. Geophys J Int 224:257–270. https://doi.org/10.1093/gji/ggaa453

Lahtinen S, Jivall L, Häkli P et al (2021) Updated GNSS velocity solution in the Nordic and Baltic countries with a semi-automatic offset detection method. GPS Solut 26:12. https://doi.org/10.1007/s10291-021-01194-z

Lian L, Wang J, Huang C et al (2018) Weekly inter-technique combination of SLR, VLBI, GPS and DORIS at the solution level. Res Astron Astrophys 18:119. https://doi.org/10.1088/1674-4527/18/10/119

Mao A, Harrison CGA, Dixon TH (1999) Noise in GPS coordinate time series. J Geophys Res: Solid Earth 104:2797–2816. https://doi.org/10.1029/1998jb900033

Najder J (2020) Automatic detection of discontinuities in the station position time series of the reprocessed global GNSS network using bernese GNSS software. Acta Geodynamica Et Geomaterialia 17:439–451. https://doi.org/10.13168/Agg.2020.0032

Ostini L, Dach R, Schaer S, et al. (2008). FODITS: A new tool of the Bernese GPS software to analyze time series. In: EUREF Symposium 2008, Brussels, Belgium. https://www.researchgate.net/publication/237596296

Perfetti N (2006) Detection of station coordinate discontinuities within the Italian GPS Fiducial Network. J Geodesy 80:381–396. https://doi.org/10.1007/s00190-006-0080-6

Teunissen PJG (1985) Quality control in geodetic networks. In: Grafarend EW, Sansò F (eds) Optimization and Design of Geodetic Networks. Springer, Berlin, pp 526–547. https://doi.org/10.1007/978-3-642-70659-2_18

Teunissen PJG (1990) Quality control in integrated navigation systems. IEEE Aerosp Electron Syst Mag 5:35–41. https://doi.org/10.1109/62.134219

Teunissen PJG (1998) Quality control and GPS. In: Teunissen PJG, Kleusberg A (eds) GPS for Geodesy. Springer, Berlin, pp 271–318

Teunissen PJG (2017) Distributional theory for the DIA method. J Geodesy 92:59–80. https://doi.org/10.1007/s00190-017-1045-7

Vitti A (2012) Sigseg: a tool for the detection of position and velocity discontinuities in geodetic time-series. GPS Solut 16:405–410. https://doi.org/10.1007/s10291-012-0257-9

Wang L, Herring T (2019) Impact of estimating position offsets on the uncertainties of GNSS site velocity estimates. J Geophys Res: Solid Earth 124:13452–13467. https://doi.org/10.1029/2019jb017705

Williams SDP (2003a) The effect of coloured noise on the uncertainties of rates estimated from geodetic time series. J Geodesy 76:483–494. https://doi.org/10.1007/s00190-002-0283-4

Williams SDP (2003b) Offsets in Global Positioning System time series. J Geophys Res: Solid Earth 108:13. https://doi.org/10.1029/2002jb002156

Williams SDP, Bock Y, Fang P et al (2004) Error analysis of continuous GPS position time series. J Geophys Res: Solid Earth 109:412. https://doi.org/10.1029/2003jb002741

Wu D, Yan H, Yuan S (2018) L1 regularization for detecting offsets and trend change points in GNSS time series. GPS Solut 22:5. https://doi.org/10.1007/s10291-018-0756-4

Yang L, Shen Y, Li B et al (2021) Simplified algebraic estimation for the quality control of DIA estimator. J Geodesy 95:15. https://doi.org/10.1007/s00190-020-01454-9

Zaminpardaz S, Teunissen PJG (2019) DIA-datasnooping and identifiability. J Geodesy 93:85–101. https://doi.org/10.1007/s00190-018-1141-3

Zhang J, Bock Y, Johnson H et al (1997) Southern California permanent GPS geodetic array: error analysis of daily position estimates and site velocities. J Geophys Res: Solid Earth 102:18035–18055. https://doi.org/10.1029/97jb01380

Jin Zhang is a PhD candidate at ShanghaiTech University and Shanghai Astronomical Observatory, Chinese Academy of Sciences, Shanghai, China. His current research mainly focuses on time series analysis and terrestrial reference frame.

Lizhen Lian is an associate professor at the Shanghai Astronomical Observatory, Chinese Academy of Sciences, Shanghai, China. Her main research interests include time series analysis and terrestrial reference frame.

Chengli Huang is a professor at the Shanghai Astronomical Observatory, as well as Prof. at ShanghaiTech University and Univ. of Chinese Academy of Sciences. His research focuses on Earth rotation, physics of the Earth interior, and terrestrial reference frame.

Cancan Xu is a PhD candidate at the Shanghai Astronomical Observatory, Chinese Academy of Sciences, Shanghai, China. His current research mainly focuses on time series analysis and digital signal processing.

Simeng Zhang is a PhD candidate at the Shanghai Astronomical Observatory, Chinese Academy of Sciences, Shanghai, China. His main research interests are time series analysis and terrestrial reference frame.